Single-Crystal Apatite Nanowires Sheathed in Graphitic Shells: Synthesis, Characterization, and Application

Namjo Jeong,[†,¶] Misun Cha,[§] Yun Chang Park,[⊥] Kyung Mee Lee,[∥] Jae Hyup Lee,[∥] Byong Chon Park,[#] and Junghoon Lee[‡,§,*]

[†]Energy Materials and Convergence Research Department, Korea Institute of Energy Research, 71-2 Jang-dong, Yuseong-gu, Daejeon 305-343, Republic of Korea, [‡]School of Mechanical and Aerospace Engineering and [§]Interuniversity Semiconductor Research Center, Seoul National University, 1 Gwanak-ro, Gwanak-gu, Seoul 151-744, Republic of Korea, [⊥]Materials and Analysis Division, National Nanofab Center, 291 Daehak-ro, Yuseong-gu, Daejeon 305-806, Republic of Korea, [∥]Department of Orthopedic Surgery, College of Medicine, Seoul National University, SMG-SNU Boramae Medical Center, 39, Boramae Gil, Dongjak-Gu, Seoul 156-707, Republic of Korea, [¶]Jeju Global Research Center, Korea Institute of Energy Research, 200, Haemajihaean-ro, Gujwa-eup, Jeju Special Self-Governing Province, 695-971, Republic of Korea, and [#]Length Group, Korea Research Institute of Standards and Science, 267 Gajeong-ro, Yuseong-gu, Daejeon, 305-340, Republic of Korea

ABSTRACT Vertically aligned one-dimensional hybrid structures, which are composed of apatite and graphitic structures, can be beneficial for orthopedic applications. However, they are difficult to generate using the current method. Here, we report the first synthesis of a single-crystal apatite nanowire encapsulated in graphitic shells by a one-step chemical vapor deposition. Incipient nucleation of apatite and its subsequent transformation to an oriented crystal are directed by derived gaseous phosphorine. Longitudinal growth of the oriented apatite crystal is achieved by a vapor–solid growth mechanism, whereas lateral growth is suppressed by the graphitic layers formed through arrangement of the derived aromatic hydrocarbon molecules. We show that this unusual combination of the apatite crystal and the graphitic shells can lead to an excellent osteogenic differentiation and bony fusion through a programmed smart behavior. For instance, the graphitic shells are degraded after the initial cell growth promoted by the graphitic nanostructures, and the cells continue proliferation on the bare apatite nanowires. Furthermore, a bending experiment indicates that such core–shell nanowires exhibited a superior bending stiffness compared to single-crystal apatite nanowires without graphitic shells. The results suggest a new strategy and direction for bone grafting materials with a highly controllable morphology and material conditions that can best stimulate bone cell differentiation and growth.

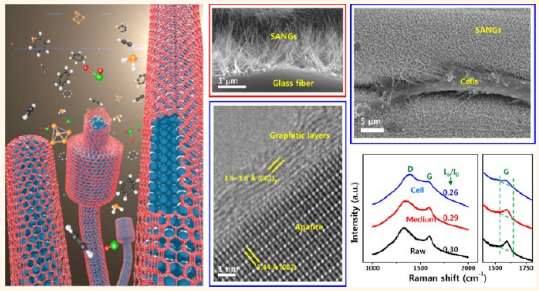

KEYWORDS: apatite · biomaterials · graphitic layer · human mesenchymal stem cells · nanowires · vapor–solid growth

Apatite has been widely used for a variety of biomedical applications due to its chemical resemblance to the mineral component of bone, excellent biocompatibility, and osteoconductivity.[1,2] Also, graphitic surfaces with a wide range of characteristics have shown a variety of desirable biomaterial properties, including a lack of cytotoxicity, lack of inflammatory induction, and maintenance of cell integrity.[3] Carbon nanotubes (CNTs) are of particular interest because they have diameters of approximately 10–100 nm, which is similar to the physical dimensions of extracellular matrix proteins, as well as excellent reinforcing properties such as high aspect ratio, high strength, and stiffness. In this respect, vertically aligned carbon surfaces are particularly promising for tissue regeneration.[4,5]

Thus, hybridization of apatite and graphitic structures that has been achieved by physical blending and *in situ* formation is a subject that is expected to drive significant advances in biomedical fields.[6–10] In these current methods, chemically modified graphitic structures are generally considered to be a passive template for apatite support or formation. These integrated structures can provide enhanced mechanical stability, whereas poor uniformity and controllability still remain to be solved. Recent efforts to find the optimum fabrication of such hybrid

* Address correspondence to jleenano@snu.ac.kr.

Received for review December 14, 2012 and accepted June 11, 2013.

Published online June 11, 2013
10.1021/nn305767t

structures are focused on the simultaneous formation of apatite and graphitic structures in a one-step process, which will be a big challenge that can overcome these problems as well as provide new opportunities in clinical applications. However, current approaches hardly achieve this target feature because of the lack of a systematic synthesis technology.[6−10] Furthermore, this simultaneous formation has never been successful in the conventional methods for apatite synthesis that involve low temperature in aqueous solution[11,12] and the *in situ* filling process that has been applied to the synthesis of filled-carbon nanotubes.[13] Particularly, the vapor−liquid−solid mechanism may not induce this simultaneous formation because apatite has a stable solid-phased structure even at high temperatures as well as extremely low carbon solubility and poor graphitization ability.[11] Thus, *in situ* hybrid formation of apatite and graphitic structures requires a novel approach.

In this study, we developed a single-step chemical vapor deposition (CVD) process to synthesize a vertically aligned single-crystal apatite nanowire sheathed in graphitic shells (SANGs). The key to achieving our approach is the role of gaseous aromatic compounds derived from PH_3 and C_2H_2 in the one-dimensional vapor−solid (VS) growth of the oriented apatite nanowires and the graphitization on the apatite's surface. Gaseous phosphorine was particularly important for the continuous VS growth on the (001)-plane-oriented apatite nanowires. The formation of graphitic layers contributed to the rearrangement of aromatic hydrocarbon molecules on the surface of the apatite and suppressed lateral growth during the longitudinal growth of the apatite nanowires. As a demonstration for a practical application, we explore the use of SANGs as a bone grafting material. To understand the mechanical health of SANGs, we also compare the bending behavior of nanowires according to the presence and absence of graphitic shells.

RESULTS AND DISCUSSION

Synthesis and Characterization of SANGs. Along the entire length of an amorphous calcium-rich glass fiber, vertically aligned SANGs of ~5 μm length grew with uniform and dense coverage (Figure 1a,b). High-resolution transmission electron microscopy (HRTEM) and fast Fourier transform (FFT) images of SANG with a diameter of approximately 15 nm clearly showed that the core corresponding to the single-crystal hexagonal apatite grew along the (001) plane (Figure 1c). A representative energy-dispersive X-ray (EDX) spectrum showed the expected Ca, P, O, and C. The Ca/P ratio of the SANGs was calculated to be approximately 1.6 (Figure 1d). The core was surrounded by discontinuous graphitic layers (Figure 1e). According to the electron energy loss spectroscopy (EELS) spectrum at the periphery of a SANG (the red square in Figure 1e), only the C-K shell ionization edge was detected (Figure 1f). At the center of the SANG (the red circle of Figure 1e), on the other hand, P-$L_{2,3}$, C-K, Ca-$L_{2,3}$, and O-K shell ionization edges were recorded at approximately 132, 284, 347, and 531 eV, respectively (Figure 1g).

A selected area electron diffraction (SAED) pattern, corresponding to the TEM image of SANGs that were dispersed on an amorphous carbon-coated Cu grid, showed families of reflections corresponding to those of hexagonal apatite (Figure 2a,b).[11] Raman spectra indicate low crystallinity of the graphitic shells and excited spectrum of the apatite core at a higher power laser (Figure 2c). At 1.25 mW, we observed two strong peaks at 1350 cm^{-1} corresponding to the D-band, which indicates the level of disordered carbon in the product, and at 1590 cm^{-1} corresponding to the G-band, which represents the width of the structural defects along the tube wall.[14] However, the peaks related to the apatite core did not appear in this spectrum. When the laser power was increased to 5 mW, a very weak peak appeared at 961 cm^{-1} corresponding to PO_4^{3-} (ν_1), which can generally be identified as the main peak of the apatite in Raman spectroscopy analysis.[10] The infrared spectroscopy shows strong phosphate and very weak hydroxyl bands (Figure 2d).[15] The υ_1 vibration (symmetric stretching) of the PO_4^{3-} groups of the apatite was detected at 963 cm^{-1}, and the υ_3 vibration (asymmetric stretching) was detected at 1031 and 1093 cm^{-1}. The υ_4 vibration (asymmetric bending) was observed at 603 cm^{-1}. Additionally, very weak peaks at 638 (a vibrational mode) and 3567 cm^{-1} (a stretching mode) were also observed. The band recorded at 1570 cm^{-1} represents the graphite-like E_{1u} mode.[16] We observed the D-band and the υ_3 vibration (asymmetric stretching) of CO_3^{-2} at ~1430 and 1450 cm^{-1}, respectively.[15,16] X-ray photoelectron spectroscopy showed the deconvolution of the C 1s, confirming the main contribution of the sp^2-hybridized C−C bond to the formation of the graphitic shells (Supporting Information Figure S1a,b). Close inspection of the Ca 2p, P 2p, and O 1s peaks showed the binding energy positions of the core elements corresponding to the apatite (Figure S1c−e).[17]

Gas Analysis and Growth Mechanism. Thermal pyrolysis in the presence of both C_2H_2 and PH_3 yields various gaseous species that are essential for the SANG growth: aromatic hydrocarbon molecules, P_4, phosphorine (C_5H_5P), and phosphinoline (C_9H_7P) (Figure S2).[18] In particular, phosphorine, a predominant derivative in this work, is known as a noncollagen macromolecule with high calcium-binding capacity and strong phosphate-solubilizing fertility.[19−21] The reaction of phosphorine on the surface of calcium-rich glass fibers may result in a phosphorine−Ca^{2+} complex, producing a molecular species that favorably bound to the phosphate generated through reaction of the derived P_4.[22,23] These phosphate-binding molecular species

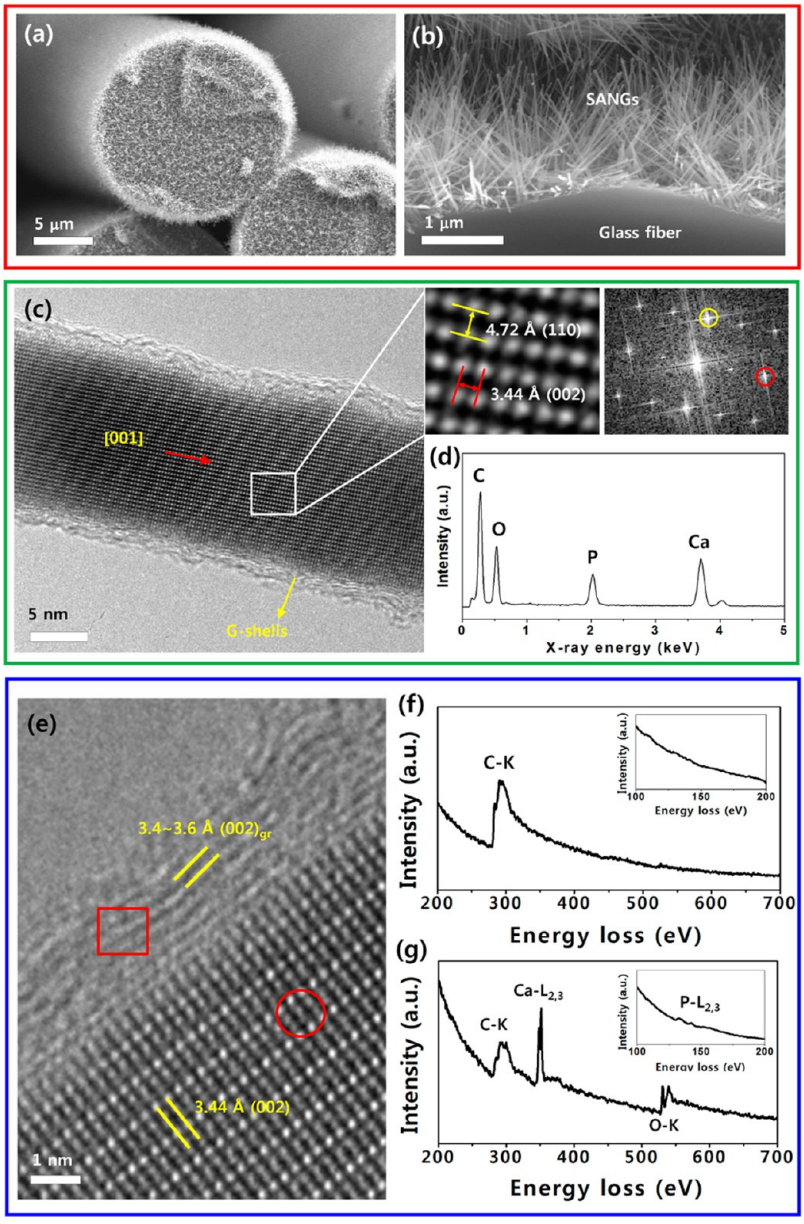

Figure 1. (a) Scanning electron microscopy (SEM) image of amorphous calcium-rich glass fibers covered with SANGs. (b) Cross-sectional image of a glass fiber with SANGs. (c) HRTEM and FFT images of SANG. Lattice spacings of the core were calculated to be 3.44 and 4.72 Å, which can be assigned to the (002) and (110) planes corresponding to the hexagonal apatite. (d) EDX spectrum of SANGs. (e) HRTEM image taken at the interface between apatite core oriented to the (001) plane and graphitic shells with lattice spacing in the range of 3.4−3.6 Å. EELS spectra acquired at the periphery (f) and the center (g) of SANG.

may promote formation of amorphous calcium phosphate compounds that are eventually transformed into the apatite crystal.[11,24,25] Growth over the initial 30 s showed the formation of both amorphous and crystalline calcium phosphate nanoparticles (Figures 3a and S3a). After 120 s, most nanoparticles changed into crystals and some slowly started to elongate (Figures 3b and S3b). On the other hand, if only C_2H_2 was supplied, no nanostructure was observed (Figure S4a−c). Supplying PH_3 alone induced the formation of amorphous nanoparticles (Figure S4d−f),[23] but crystallization of the amorphous nanoparticles did not occur even after the gas supply was switched to C_2H_2 after initial exposure to PH_3 (Figure S4g−i). When both C_2H_2 and PH_3 were supplied, the growth of well-defined nanowires was precipitated (Figure S4j−l).

A continuous supply of gaseous Ca-[26] and P-related species initiated the growth of the apatite crystals. In the proposed gas-phased reaction system, CaOH(g) and $Ca(OH)_2$(g) produced from CaO(s) in the presence of H_2 and H_2O may be more dominant than Ca(g) and CaO(g) that can be sublimated or dissociated. Also, the derived P_4 may react with O_2(g), resulting in phosphorus pentoxide, P_4O_{10}. Based on the available molecules, the vapor−solid growth of apatite crystals can be hypothesized as

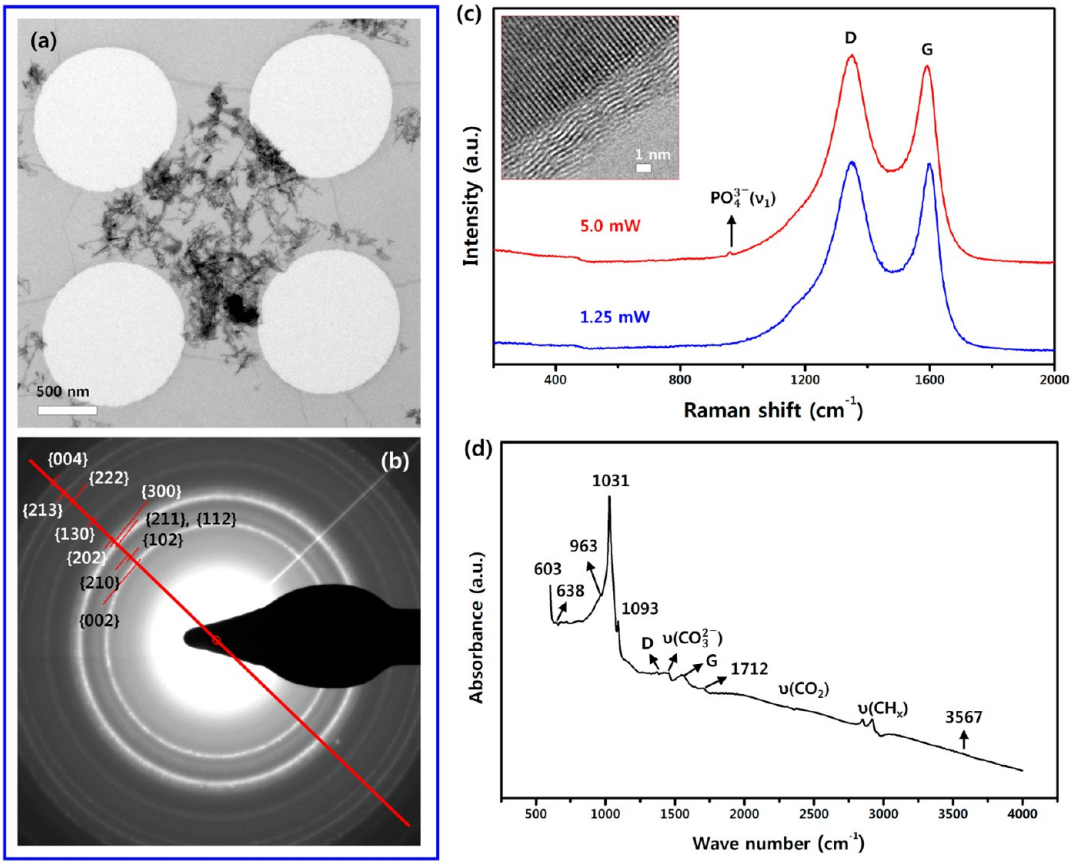

Figure 2. (a) TEM image of SANGs. (b) Corresponding SAED pattern with the peaks labeled with Miller indices. (c) Raman spectra of SANGs measured at an energy power of 1.25 (blue) and 5.0 mW (red). Inset is a TEM image showing core−shell configuration of SANGs. (d) Infrared spectrum of SANGs.

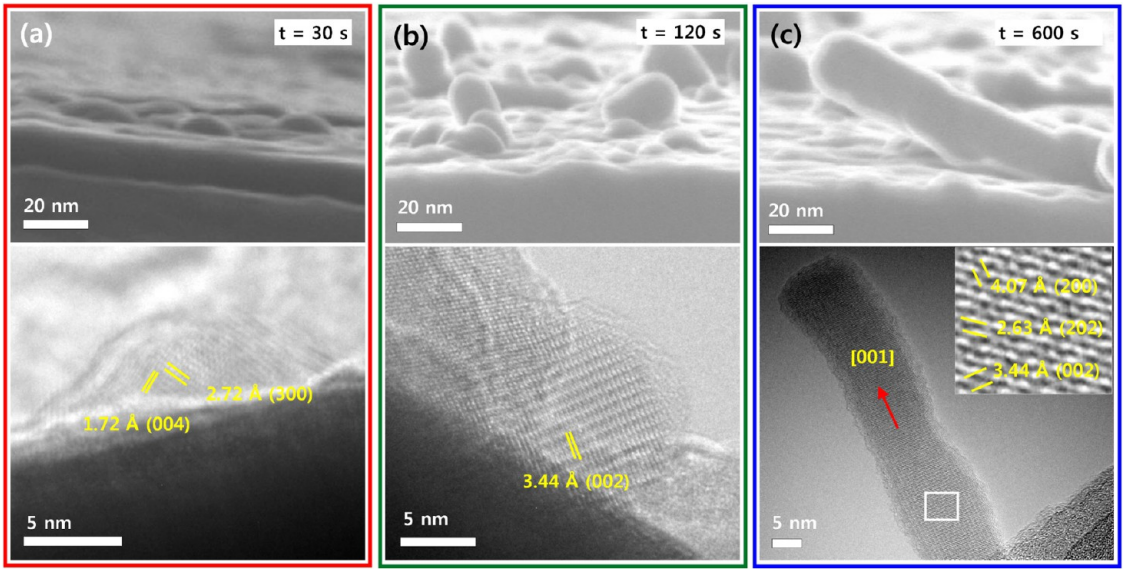

Figure 3. (a) Exposure to both C_2H_2 and PH_3 for 30 s at 750 °C induced formation of nanoparticles in the range of 10−20 nm on the surface of a glass fiber. Some amorphous nanoparticles were also observed in the same samples (Figure S3a). (b) Nanoparticles completely crystallized after 120 s. (c) Complete transformation of nanoparticles into nanowires after 600 s.

follows: $10Ca(OH)_2(g) + 1.5P_4O_{10}(g) = Ca_{10}(PO_4)_6(OH)_2(s) + 9H_2O(g)$. On the other hand, $H_2O(g)$ may react with the gaseous P_4O_{10}, resulting in gaseous H_3PO_4 ($P_4O_{10}(g) + 6H_2O(g) = 4H_3PO_4(g)$). Therefore, another route of chemical reaction for the gas-phased formation of apatite crystals can be as follows: $10Ca(OH)_2(g) + 6H_3PO_4(g) = Ca_{10}(PO_4)_6(OH)_2(s) + 18H_2O(g)$. Surprisingly, all the crystalline apatite nanoparticles were transformed

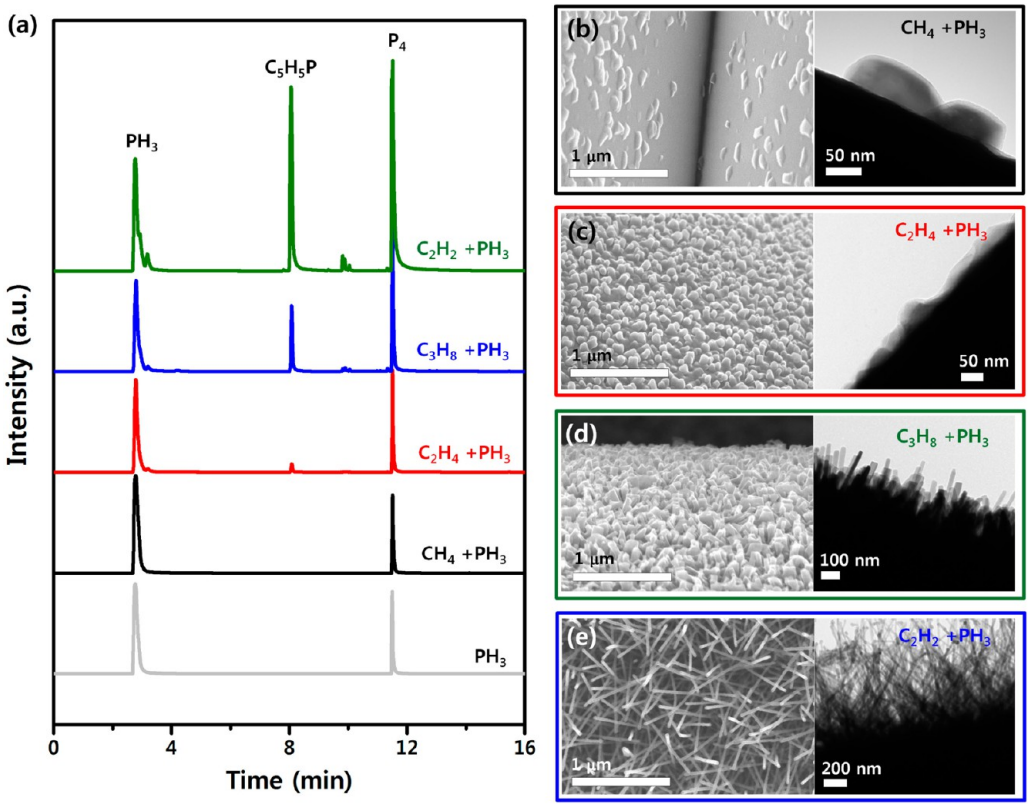

Figure 4. (a) Gas chromatography nitrogen phosphorus detector (GC-NPD) results obtained from experiments performed in the presence of different reactants in the absence of a calcium-rich glass substrate at 750 °C: PH_3 only, $CH_4 + PH_3$, $C_2H_4 + PH_3$, $C_3H_8 + PH_3$, and $C_2H_2 + PH_3$. Microscopic images of nanostructures observed on the surface of the glass fiber with different reactants at 750 °C: (b) $CH_4 + PH_3$, (c) $C_2H_4 + PH_3$, (d) $C_3H_8 + PH_3$, and (e) $C_2H_2 + PH_3$.

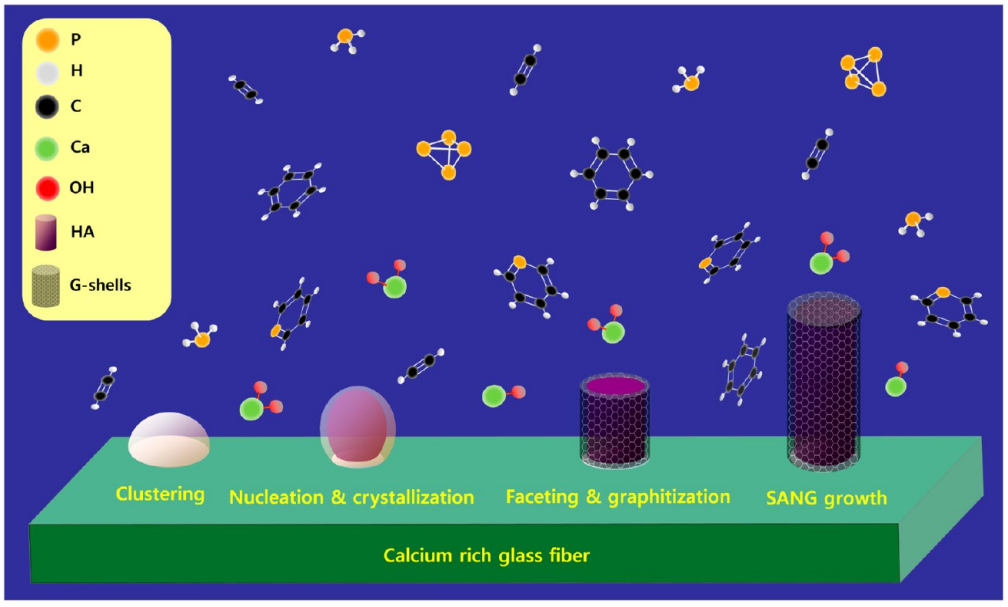

Figure 5. Schematic of growth mechanism: clustering, nucleation and crystallization of amorphous nanoparticles, faceting of apatite and formation of graphitic shells, and SANG growth.

into nanowires oriented in the (001) plane along the longitudinal axis (Figure 1c). We speculate that the phosphorine leads to more favorable interactions with Ca^{2+} and phosphate ions on the (001) plane as compared to other planes, such as (100) and (010) planes, resulting in an increase in the interfacial energy and instability of the (001) plane.[27−30] To minimize the total interfacial energy of the apatite crystals, the oriented growth of the apatite crystal should be maintained in the (001) plane. Also, it is noteworthy that, during the growth process of

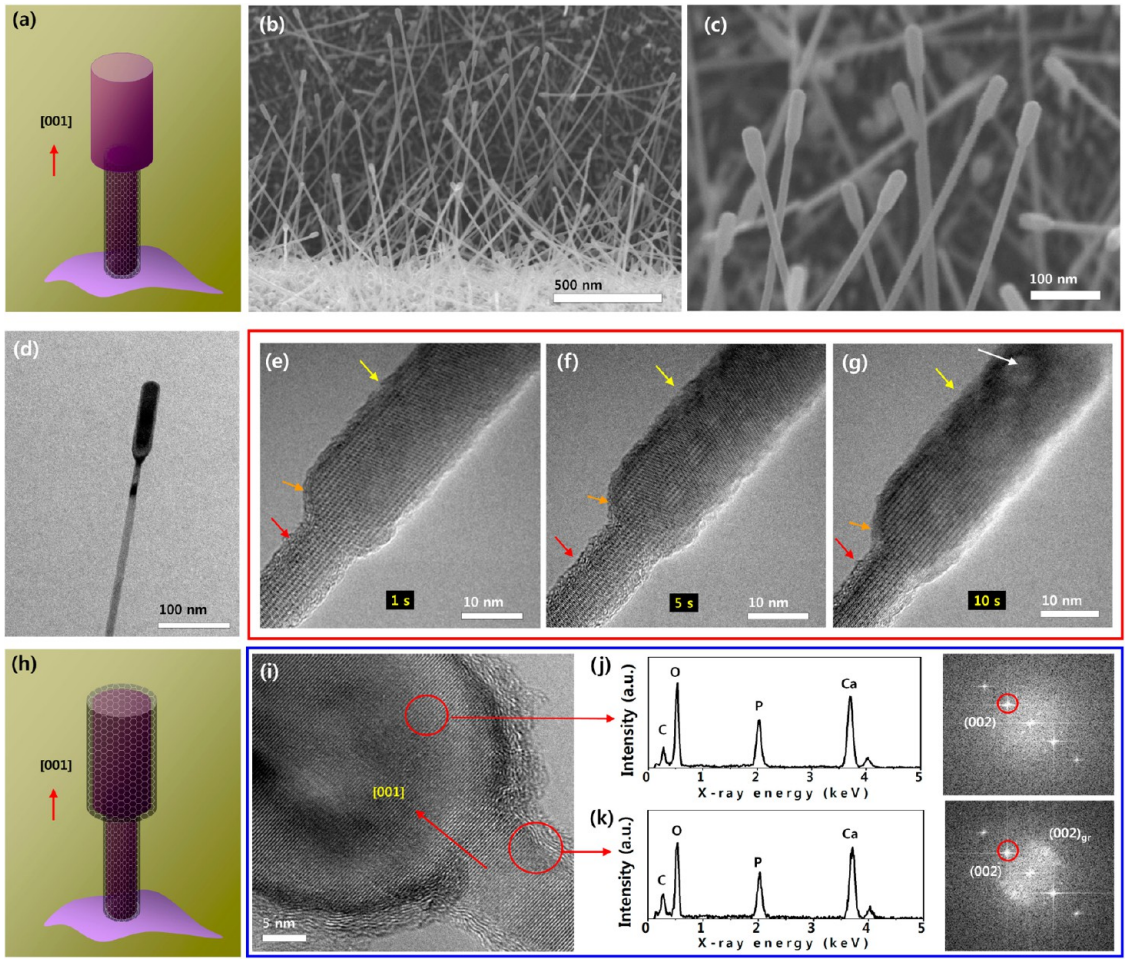

Figure 6. (a) Schematic illustrating the enlarged head without graphitic shells. (b) Low- and (c) high-magnification SEM images. (d) TEM images. (e−g) HRTEM images of SANG obtained with increasing electron beam exposure time: 1, 5, and 10 s at an accelerating voltage of 200 kV. Red arrow, stem surface of a SANG. Orange arrow, neck surface of a SANG. Yellow arrow, head surface of a SANG. (h) Schematic illustrating the enlarged head with graphitic shells. (i) HRTEM image observed at the neck of a SANG orientated in the [001] direction. The graphitic shells were formed on the whole surface of the apatite nanowire. (j,k) Energy-dispersive X-ray spectroscopy (EDX) spectra and FFT images corresponding to the red circles selected in (i). The $(002)_{gr}$ lattice plane was consistent with that of bulk graphite.

apatite nanowires, impurities such as fluoride and carbonate ions can be partially substituted in the phosphate and/or hydroxyl sites of a typical apatite structure, particularly at high temperature. This prediction is strongly supported by the infrared spectroscopy that displays very weak hydroxyl peaks and the existence of a carbonate peak (Figure 2d).

Graphitic layers were simultaneously formed along the relatively stable surface of the apatite crystals and eventually prevented the deposition of the gaseous sources on the radial surface, thus suppressing lateral growth. It is unlikely that the formation of the graphitic layers was promoted by a direct decomposition of C_2H_2 on the apatite crystal because of the substantially poor catalytic activity of the apatite. Rather, it is possible that the radial surface of the apatite nanowire provided an interface where the derived aromatic hydrocarbon molecules were rearranged into nuclei for the formation of the graphitic layers.[31−35] Then, the growth process continued with the addition of the aromatic hydrocarbon molecules and the elongation of the apatite nanowire. Thicker graphitic layers were observed at higher synthesis temperatures (Figure S5). The concentration of polycyclic aromatic hydrocarbon molecules should increase at elevated temperatures (Figure S6) and promote the enormous surface accumulation of graphitic fragments for the formation of thick graphitic layers. By 600 s, the nanoparticles were completely transformed into nanowires (Figure 3c).

Gas analyses for thermal pyrolysis performed in the presence of PH_3 and different hydrocarbon sources indicated that the precipitated formation of phosphorine was favored to occur in the order $C_2H_2 > C_3H_8 > C_2H_4 > CH_4$ at 750 °C (Figure 4a). Clearly, aromatization of hydrocarbons is an essential process for evolution of gaseous phosphorine. Use of CH_4 (Figure 4b) or C_2H_4 (Figure 4c) led to the formation of nanoparticles instead of nanowires. On the other hand, supplying C_3H_8 (Figure 4d) facilitated the formation of nanowires and especially C_2H_2 (Figure 4e) from which vigorous

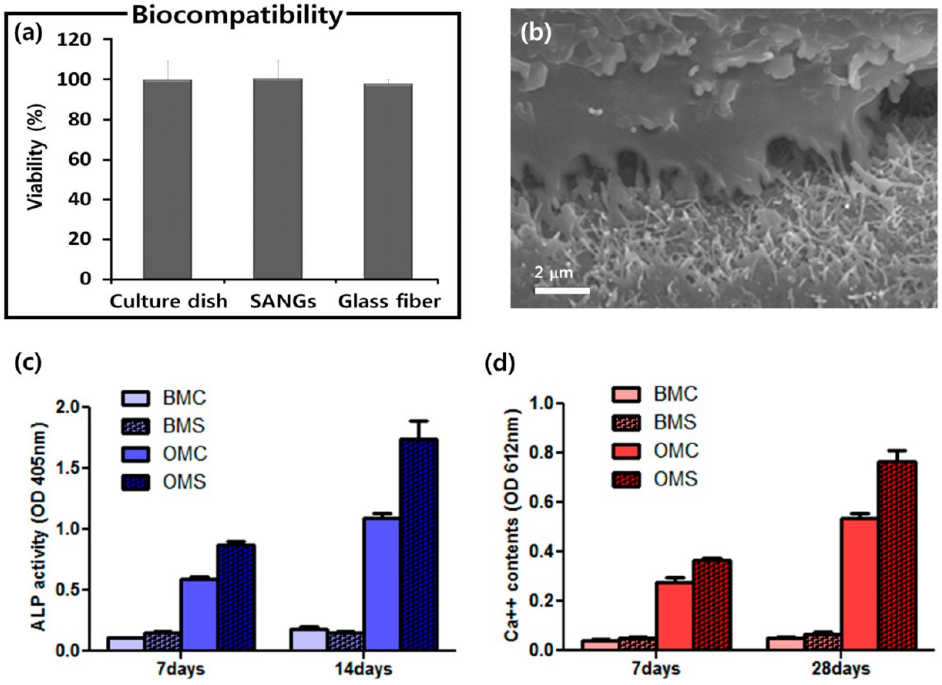

Figure 7. (a) Biocompatibility of the prepared scaffold was determined by colorimetric MTS assay in a 7 day culture on a prepared substrate. SEM images of the production of mineral particles by hMSCs on the culture dish. (b) SEM image showing cell extensions. (c) ALP activity and (d) calcium level at four different combinations of substrates and induction media: basal medium + culture dish (BMC), basal medium + SANGs (BMS), osteogenic medium + culture dish (OMC), and osteogenic medium + SANGs (OMS).

generation of phosphorine was observed. These results confirmed that phosphorine drives the incipient nucleation and crystallization of apatite as well as provides an oriented facet where the apatite crystals can grow to nanowires *via* the VS mechanism. On the basis of our experimental observations, we proposed the growth mechanism of the SANGs as shown in Figure 5 (movie S1).

Controlled Growth of SANGs. To further verify our proposed mechanism, we performed two tests. In the first test (Figure 6a), after the growth using both PH_3 and C_2H_2, the C_2H_2 supply was cut off for a short duration, and then the PH_3 supply was also cut off. SANGs with bare enlarged head portions were synthesized as shown in Figure 6b−d. Length and diameter of the head were in the range of 50−100 and 30−50 nm, respectively. This feature is attributed to suppression of surface graphitization after supply of C_2H_2 ceases, resulting in the surplus deposition of the gaseous Ca- and P-related sources on the radial surface. Unlike the stem enclosed by graphitic layers, some debris was partially formed on the head after the prolonged exposure to the electron beam during TEM investigation (Figure 6e−g) because of the ejection of hydroxyl ions due to high sensitivity of the hydroxyapatite to electron beams.[36] The second test was conducted by resupplying only C_2H_2 after cutting off the PH_3 supply that is the last step in the first test (Figure 6h). Complete sheathing of the head's surface with graphitic layers was observed in Figure 6i. This proved the role of the aromatic hydrocarbon molecules in the surface graphitization on the apatite. Crystallographic and integrant characteristics of the apatite revealed that there was no significant morphological and structural change after the two tests (Figure 6j,k).

SANGs Induce Osteogenic Response of hMSCs through a Programmed Smart Behavior. Next, we tested the ability of the SANGs-on-glass fiber to serve as a biological scaffold material for osteogenic differentiation using human mesenchymal stem cell (hMSC, Figure S7). An MTS assay performed after 7 days of culture on the prepared SANGs scaffold showed no significant toxic effect on the hMSCs viability compared with that on a culture dish (Figure 7a). An effective initial growth was verified by the cytoplasmic extension of cells attached to the surface of the scaffolds and secondary extensions spreading across the tips of the SANGs (Figures 7b and S8). Hydrophobic surface of SANGs with appropriate nanotopography favors protein adsorption, and this surface property of SANGs may successively support cell attachment and proliferation.[37−39]

We investigated the role of the SANGs scaffold in the guided differentiation of the hMSCs into osteoblasts. Alkaline phosphatase (ALP) activity, an early marker of osteogenic differentiation, can be used as an indicator for differentiation efficiency. Figure 7c,d compares the ALP activity and calcium level at four different combinations of substrates and induction media: basal medium + culture dish (BMC), basal medium + SANGs (BMS), osteogenic medium + culture dish (OMC), and

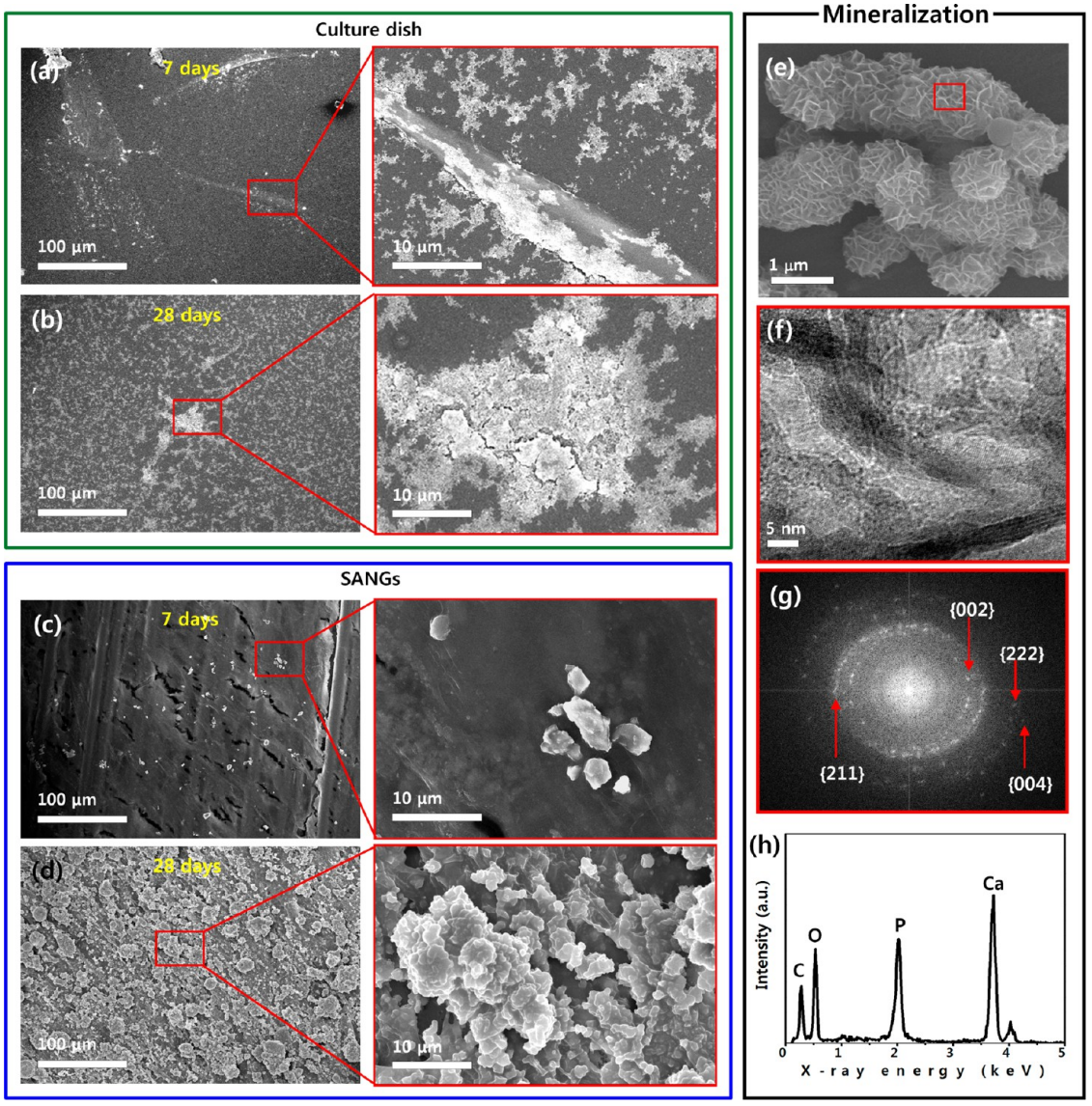

Figure 8. SEM images of the production of mineral particles by hMSCs on the culture dish (a,b) and SANG scaffold (c,d) after culture for 7 and 28 days. (e) SEM and (f) HRTEM images of as-formed minerals. (g) FFT image showing {002}, {211}, {222}, and {004} families of reflections corresponding to those of hexagonal apatite. (h) Expected Ca, P, and O, and the Ca/P ratio consistent with that of hydroxyapatite.

osteogenic medium + SANGs (OMS). It has been previously shown that the nanotopographical features alone can enable the osteogenic differentiation without the use of an osteogenic medium that contains dexamethasone as a differentiation factor.[40,41] These exciting results, however, required elaborate optimization processes to find topographical features such as size, spacing, and distribution symmetry that best induces the directed differentiation. In our case, such optimization needs yet to be carried out to achieve the maximum level of differentiation efficiency on the SANGs. Nevertheless, the comparison between BMS and BMC indicates that the early differentiation efficiency on the SANGs (7 days) was higher than that on the culture dish. This effect is more pronounced when the osteogenic medium (10 nM dexamethasone, 10 mM β-glycerophosphate, and 100 μM ascorbic acid-2-phosphate) was used. OMS ALP activity was improved by ~50% compared to OMC case. This enhancement in the differentiation efficiency is directly translated into the highest calcium level in the 28 day culture of the hMSC in OMS. It should also be noted that none of the previous research demonstrated that the efficiency of topographically driven differentiation alone can exceed that of the differentiation in an osteogenic medium.[40,41]

The enhancement of differentiation on the SANGs scaffold is elucidated by the nanotopographical incentives with pillar-like structures that stimulate the differentiation process in a similar manner studied in the previous works.[40−42] Current SANGs nanowires are randomly grown to form a "mat" arrangement whose individual sizes are ~20 nm in diameter and ~200 nm in spacing. Previous studies show that the

nanotopographical stimulus alone can drive the differentiation efficiency up to the level of the culture dish in osteogenic medium. More optimization is necessary in the future because the BMS efficiency is far lower than the OMC efficiency in our case. The critical features of the pillar-like structures such as diameter, height, and distribution can be optimized through the control of deposition conditions as demonstrated in this work.

Improved differentiation and further growth resulted in the substantial increase in the mineral production compared to that on a culture dish. After 7 days of culture, the cells on the SANGs induced a higher deposition of bone-like mineral. A dramatic course of mineralization was observed over 28 days of culture; remarkably, the surface of the SANGs was completely covered with a layer of mineral particles (Figure 8c,d). In contrast, we found a relatively small amount of mineral particles scattered over the culture dish (Figure 8a,b). SEM, TEM, FFT, and the EDX spectrum analyses on the mineral product on the SANGs showed the hallmark of hexagonal hydroxyapatite (Figure 8e–h).[11]

One might question the utility of the inner core apatite of the SANG in contributing to the continued growth. Previous studies showed that a well-defined graphene was not removed after the growth of hMSC.[42] Other investigations, however, indicated that graphitic layers with lower crystal quality similar to our graphitic shells may not withstand the oxidation process in an intracellular environment.[43] Indeed, our TEM images showed that the portion of the graphitic shells in contact with the cell disappeared partially or underwent a decrease in the number of shells (Figure 9a–d). Raman spectroscopy further confirmed this result (Figure 9e); the intensity of the G-band after the proliferation and differentiation of the hMSCs was reduced, resulting in a decrease of the intensity ratio of the G- to D-band (I_G/I_D). These results strongly suggest that the graphitic shells were degraded and the apatite was exposed through the interaction with the cells. Thus, initial growth and differentiation should be stimulated by the morphological effects of the SANGs specific to their topographical arrangement as well as excellent reinforcing properties such as high strength and stiffness. Later, the graphitic shells would degrade and the bare apatite core would enable the function of providing biologically compatible environments, leading to an excellent bony fusion with the mat of nanopillars. This intelligent material behavior will enable a new bone graft that can induce fast skeletal differentiation and regeneration with superior mechanical properties.

Bending Experiment of SANGs and Single-Crystal Apatite Nanowires without Graphitic Shells (SANs). The proliferation and differentiation of bone stem cells depends strongly on the mechanical strength as well as the biocompatibility of the scaffold. Much effort has been

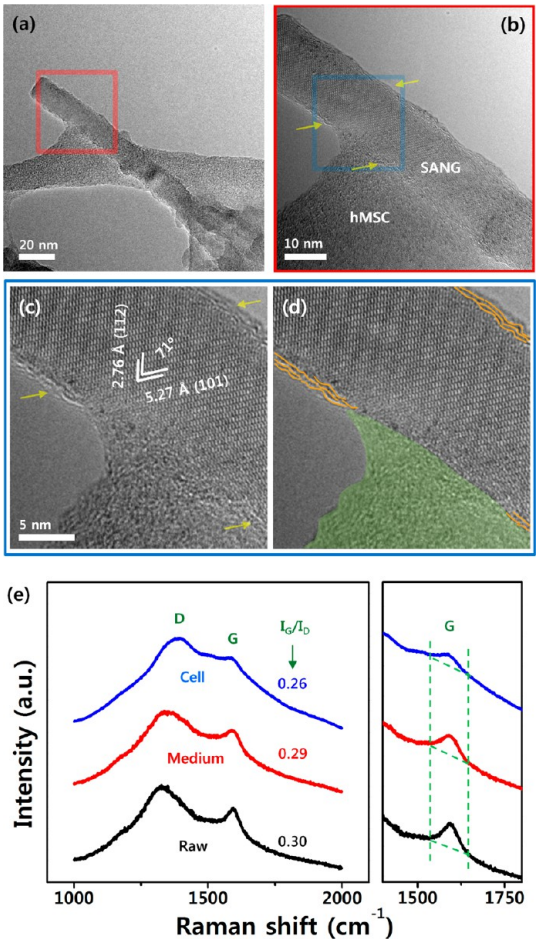

Figure 9. (a,b) TEM images showing a SANG in contact with a secondary extension of cell. (c) HRTEM image showing a portion of graphitic shells in contact with the secondary extension. (d) HRTEM image highlighting a cell (green shading) and graphitic shells (orange shading). (e) Raman spectra of raw, medium-treated, and cell-cultured SANGs (785 nm).

made to realize mechanically reinforced scaffolds but mostly limited to CNT-based apatite composites with the role of CNT as a reinforcing additive in an extra processing step.[44–46] Here, we wondered whether the graphitic layers that are systematically integrated with the apatite core in a single-step synthesis can enhance the reinforcing effect of the SANGs. For this goal, we investigated the bending behavior of individual nanowire according to the presence and absence of graphitic layers. Single-crystal apatite nanowires without graphitic layers (SANs) were additionally prepared *via* heat treatment of SANGs for 1 h at 650 °C in air. The HRTEM image clearly shows that the surface of SANs is free from the graphitic layers (Figure S9a). The FFT pattern of the SANs shows no significant change in the apatite structure after oxidizing the SANGs (Figures 1c and S9b).

The prepared SANGs and SANs were placed on the surface of the nanowire cartridge module of the SEM-based nanomanipulator (see Methods). First, we aligned an atomic force microscopy (AFM) tip with the

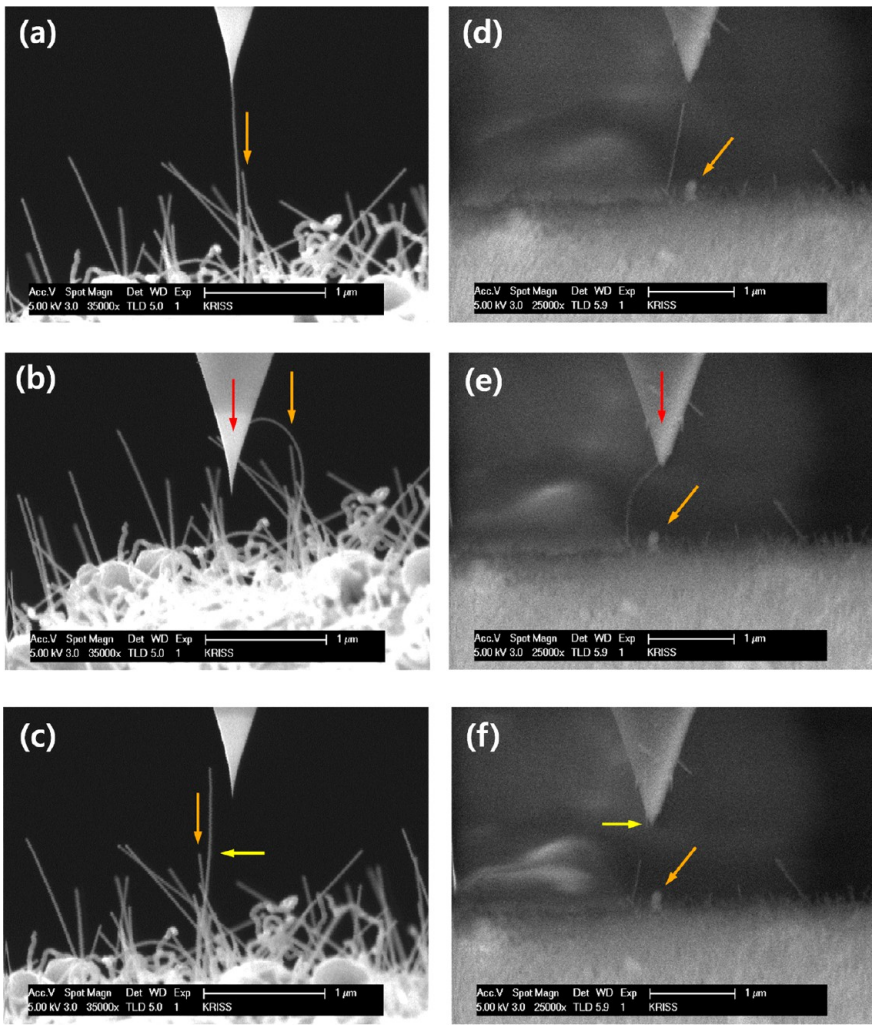

Figure 10. Bending experiment of (a–c) SANGs and (d–f) SANs nanowires using SEM-based nanomanipulator. (a,d) Alignment of the nanowire and AFT tip. (b,e) Nanowire bending by pushing the AFM tip and (c,f) nanowires after bending. It is remarkable that the SANGs nanowire restored its original shape after the large bending, while the SANs nanowire was unable to withstand the load of the AFM tip and eventually broke. Orange, red, and yellow arrows indicate reference position for observation, motion direction of the AFM tip, and final state of nanowires, respectively.

top of the individual target nanowire (Figure 10a,d). The AFM tip was further pushed down after contacting the top, inducing a large bending. The SANGs nanowire did not break after considerable bending (Figure 10b) and returned to its original shape when the AFM tip was detached (Figure 10c). This result demonstrates an excellent mechanical strength similar to that of CNT.[47,48] On the other hand, the SANs nanowire could not withstand such harsh load and eventually fractured (Figure 10e,f). This inherent brittleness of the apatite crystal is a well-known issue against reliable coating for a practical bone grafting. We obtained similar results on repeated tests. These results manifest the function of the graphitic structure sheathing apatite nanowire in providing mechanical reinforcement.

Study of the detailed mechanism and quantitative analysis will be an exciting future work. For instance, we do not know what happened to the inner core crystal when the SANGs nanowire went through the large deformation. Did it break but remain in the core retained by the graphtic shell? Did it restore the crystal structure on returning to its original shape? Did it never break due to the intermolecular binding force at the interface between the crystal surface and the graphitic inner layer? One of the most critical pieces of information relevant to the current work is that the SANGs structure enables a reliable material structure that consistently provides proper environment when cells grow on it.

CONCLUSION

We have demonstrated a single-step CVD technique to synthesize a vertically aligned SANG. Gaseous phosphorine is a key component for the continuous VS growth of (001)-plane-oriented apatite nanowires. Lateral growth of apatite nanowires along longitudinal growth and formation of graphitic layers are highly

controllable. The concept of apatite nanostructure sheathed in graphitic layers is extended to the encapsulation of other type of apatite [$X_{10}(Y)_6Z_2$] (Figure S10).[11] Moreover, our CVD technique is reproducible in various forms such as *in situ* coating or powder, thus proving a general strategy for fabricating a broad variety of artificial scaffolds and opening up new possibilities for practical applications. We consider that our SANGs are likely to be useful scaffold materials for hMSC-based tissue engineering strategies because they reflect the dynamic nature of many biological processes. SANGs effectively induced osteoblastic differentiation of hMSCs because of their smart structure. Moreover, we first established that the unique core–shell nanostructure of the SANGs with a high mechanical stiffness showed a programmed material behavior; the graphitic shells were degraded by the activity of hMSCs, providing a biocompatible environment in the later stage of differentiation. We therefore consider that SANGs may overcome the technical barrier to produce a hybrid nanostructure for smart interactions with biological cells.

METHODS

Material Preparation. To prepare the single-crystal apatite nanowires sheathed in graphitic shells (SANGs), glass fibers (amorphous calcium-rich glass fibers, having a diameter of approximately 15 μm and composition range of SiO_2 (62 wt %), CaO (25 wt %), Al_2O_3 (16 wt %), B_2O_3 (10 wt %), MgO (5 wt %), $Na_2O + K_2O$ (2 wt %) and impurities such as Fe_2O_3 and fluoride, obtained from Owens Corning) were assembled on a quartz plate of 10 × 10 × 1 mm^3 ($W \times L \times t$) by using tweezers to slightly push and flatten out the glass fibers that had been wetted by DI water. The fibers on the quartz plate were then dried at 100 °C. The assembled glass fiber film was less than 50 μm thick. Also, glass powders with a particle size of approximately 10 μm, which were prepared by cracking the glass fibers with a jet mill machine (belonging to the Korea Institute of Ceramic Engineering and Technology (KICET); feeding size = 120 mesh, grinding speed = 5–50 kg/h, power = 0.1 kW, air consumption = 0.12 N m^3).

SANG Formation. For the formation of the SANGs, the prepared glass samples were placed in the reactor with a quartz tube of 36 × 400 × 2 mm^3 ($D_{out} \times L \times t$). The reactor was evacuated to 10^{-3} Torr, purged with Ar or He (99.9999%, ~2000 cc/min) as a carrier gas, and then heated to the synthesis temperature (650–850 °C) at a rate of 10 °C/min. C_2H_2 (>99.9%, ~100 cc/min), CH_4 (>99.99%, ~100 cc/min), C_2H_4 (>99.9%, ~100 cc/min), C_3H_8 (>99.95%, ~100 cc/min), and PH_3/Ar or He mixture gas (PH_3 of 200–1000 ppm in Ar or He balance, >99.999%, ~100 cc/min) were used as the reactant gases. The synthesis time was controlled over the range of 30 s to 1 h. As the supply of reactants stopped, the reactor was slowly cooled to room temperature using only carrier gas.

SANG Characterization. SANGs were characterized using scanning electron microscopy (SEM; S-4700, HITACHI) operated at an accelerating voltage of 10–15 keV and transmission electron microscopy (TEM; Tecnai F30 Supertwin) operated at an accelerating voltage of 200–300 kV. Energy-dispersive X-ray spectroscopy (EDX; EDAX, Genesis) and electron energy loss spectroscopy (EELS; GATAN, Enina 1000) studies were carried out to confirm the composition of SANGs using scanning transmission electron microscopy (STEM) operated with a 1 nm beam diameter. The characteristics of graphitic layers were identified from Raman spectroscopy (JY LabRam HR, 514.5 nm line of an Ar ion laser). The energy power was controlled within the range 1.25–5 mW with a 1 μm focus spot lasting for 30 s. To characterize the chemical structures of apatite, infrared spectroscopy (IFF66 V/S and HYPERION3000) was recorded using the attenuated total reflection method over the range of 600–4000 cm^{-1}. The chemical bonds of SANGs were analyzed by high-resolution X-ray photoelectron spectroscopy (XPS; AXIS-NOVA, Kratos Inc.). The analytical area was 1 × 2 mm^2, and the base pressure was 5.0×10^{-9} Torr.

Gas Analysis. Gas chromatography (GC; 7890A, Agilent Technologies) and GC-MS (6890, Agilent Technologies and a 5973 Network) were performed to verify the growth mechanism of SANGs. A nitrogen phosphorus detector (NPD), flame ionization detector (FID), and thermal conductivity detector (TCD) were used for detecting the as-generated gas products. The operating parameters were as follows: (a) columns 30 m × 320 μm × 0.25 μm, 19091J-423 (Agilent) for the NPD; 30 m × 320 μm × 0 μm, 113–4332 (J&W Scientific) for the FID; packaged column, 12352-U (Supelco) for the TCD. (b) The initial temperature of the oven was set to 40 °C and was maintained as such for 4–6 min. This was followed by a linear increase of 20 °C/min up to the final temperature of 200–300 °C, which was maintained for 5–6 min. (c) The detector temperature was set to 325, 300, and 250 °C for the NPD, FID, and TCD experiments, respectively. (d) Gas conditions for the NPD: He at 5 mL/min, air at 60 mL/min, and H_2 at 3 mL/min; FID: He at 25 mL/min, air at 350 mL/min, and H_2 at 30 mL/min; TCD: He at 30 mL/min. (e) The temperature was set to 180 °C. (f) Rubidium beads were used for NPD. (g) Injection volume: 600 μL, auto injection, at a temperature of 250 °C. (h) Run time: 18 min. The amount of gases and glass powder used were the same as those used in the mass spectroscopy analysis. The detection range of the mass detector was from 0 to 300 *m/z*, and the scan speed was 5.62/s.

Scaffold Preparation. We prepared a scaffold installed with glass fiber SANGs as a thin film. The prepared scaffolds of 10 × 10 mm^2 ($W \times L$) were placed in a square cavity of 11 × 11 × 5 mm^3 ($W \times L \times H$) made at the center of the circular polycarbonate frame, which was 20 mm in diameter and 8 mm in thickness. Then, a square polycarbonate frame of 11 × 11 × 5 mm^3 ($W \times L \times H$) was inserted into the cavity of the circular frame. The prepared scaffolds were placed in 12-well plates and sterilized with ethylene oxide gas.

Cell Culture. Cryopreserved human mesenchymal stem cells (hMSCs) were purchased from Lonza (USA). The hMSCs were suspended in MSCGM culture medium (Lonza, USA) at 37 °C in a humidified atmosphere containing 95% air and 5% CO_2. The confluent cells were subcultured to their next passage using 0.05% trypsin-EDTA in four passages. Then the hMSCs were seeded on the surface of the prepared scaffolds at a density of 2.5×10^4 cells/scaffold.

Biocompatibility Test. To verify the biocompatibility of SANGs and SANs, we performed the MTS assay to quantify cell viability and proliferation, using the reagents and procedures outlined by the manufacturer (CellTiter 96 AQueous One solution, Promega, USA). To process samples for the MTS assay, the samples were rinsed with PBS to remove unattached cells and incubated with 20% MTS reagent in a serum-free medium for 3 h at 37 °C. The absorbance of the obtained dye was measured at 490 nm using a spectrophotometric plate reader (Bio-Rad microplate reader benchmark 10892, Hercules, CA). Cells were tested at a density of 2.5×10^4 cells/scaffold and cultured for 7 days.

Alkaline Phosphatase Activity. Samples of hMSC lysate (20 μL) were combined with 20 μL of *p*-nitrophenyl phosphate (pNPP) substrate and 160 μL of alkaline buffer solution (Sigma) in a 96-well plate and incubated for 20 min at room tempertature. We terminated the reaction by adding 180 μL of 0.05 M NaOH and obtained readings at 405 nm (Bio-Rad microplate reader benchmark 10892; Bio-Rad, Hercules, CA).

Calcium Measurement. A calcium quantification kit (Bioassay Systems, USA) was used to determine the amount of calcium deposited by hMSCs cultured on the SANG scaffolds. An acidic

extract solution for this assay was prepared by incubating all the samples with 0.1% N HCl (Sigma, USA) at room temperature. The amount of calcium present in the acidic supernatant was then spectrophotometrically quantified in accordance with the manufacturer's instructions by using a commercially available kit. The light absorbance was measured using a spectrophotometer (Bio-Rad microplate reader benchmark 10892; Bio-Rad, Hercules, CA) at 612 nm to determine calcium deposition.

SEM and TEM of Cultured Samples. SEM was used to determine the morphological characteristics of the cells attached on the substrates and identify features of as-formed minerals. After cell culture, the samples were washed with PBS, fixed with a solution of 2% glutaraldehyde, and postfixed in 1% osmium tetraoxide. The samples were then dehydrated in a graded series of alcohol (50, 70, 80, 90, 95, and 100%) and isoamyl acetate following critical-point drying. After sputter coating with Pt or Os, the cells were observed using a FE-SEM operated at an accelerating voltage of 10 keV. In addition, we observed the cell–nanowire interface and characterized the mineralized products using a TEM operated at an accelerating voltage of 200 keV.

Raman Spectroscopy of Cultured Samples. Two types of SANG scaffold samples were prepared. In the first type, hMSCs (2×10^4/well) were seeded on the SANG scaffold, and in the other type, cell-free medium was added to the scaffold. After culture for 21 days, the SANG scaffolds were washed twice with PBS and then treated with 0.2% Triton X-100 in PBS and 0.1% HCl for 5 min at room temperature. Spectra were obtained under ambient conditions by using the 785 nm line of an argon ion laser. Raman measurements were obtained using backscattering geometry with a JY LabRam HR, fitted with a liquid-nitrogen-cooled CCD detector. The energy power was set to 200 mW with a 1 μm focus spot lasting for 30 s. Results obtained from the two SANG scaffolds were compared with those obtained from the raw SANG scaffolds.

SEM-Based Nanomanipulator. The bending experiment was performed with a homemade nanomanipulator installed inside a SEM (FEI, Sirion). The nanomanipulator consists of two modules, AFM tip and nanowire cartridge modules, both having the degree of freedom of three-directional rectilinear and one-dimensional rotational motion. Each motion is driven at the precision of angstrom with the corresponding piezo-actuator (Attocube) and controlled *via* Labview program. The AFM tip is the normal noncontact mode tip (Nanosensors, NCHR) which is attached on the end face of the left module. The nanowires are placed on the surface of the nanowire cartridge module. The population density of the nanowires is so scarce that the AFM tip module in contact with a single nanowire can extend in the *Y*-axis without touching others. Thus the AFM tip can push only a single nanowire. The acceleration voltage was 5.0 kV.

Conflict of Interest: The authors declare no competing financial interest.

Acknowledgment. This research was supported by the Pioneer Research Center Program through the National Research Foundation of Korea funded by the Ministry of Education, Science and Technology (2013-008421), and also conducted under the framework of Research and Development Program of the Korea Institute of Energy Research (KIER: B2-2461-08). The authors thank Mr. K.S. Myung, Dr. G.B. Park, Mr. S.Y. Kim, and Dr. S.C. Nam (KIER), and also thank Dr. H.S. Baik of Samsung Semiconductor, Dr. Y.H. Kim of Korea Research Institute of Standards and Science, and Mr. M.S. Hyun and Dr. J.M. Yang of NNFC.

Supporting Information Available: XPS results, gas analyses (GC and GC-MS), temperature and reactant effects, scaffold preparation and cell culture, cell movement on SANGs, growth of single-crystal strontium apatite nanowires sheathed in graphitic shells. This material is available free of charge via the Internet at http://pubs.acs.org.

REFERENCES AND NOTES

1. Stevens, M. M.; George, J. H. Exploring and Engineering the Cell Surface Interface. *Science* **2005**, *310*, 1135–1138.
2. Dorozhkin, S. V.; Epple, M. Biological and Medical Significance of Calcium Phosphates. *Angew. Chem., Int. Ed.* **2002**, *41*, 3130–3146.
3. Cui, F. Z.; Li, D. J. A Review of Investigations on Biocompatibility of Diamond-like Carbon and Carbon Nitride Films. *Surf. Coat. Technol.* **2000**, *131*, 481–487.
4. Hu, J.; Shi, J.; Li, S.; Quin, Y.; Guo, Z.; Song, Y.; Zhu, D. Efficient Method To Functionalize Carbon Nnanotubes with Thiol Groups and Fabricate Gold Nanocomposites. *Chem. Phys. Lett.* **2005**, *401*, 352–356.
5. Harrison, B. S.; Atala, A. Carbon Nnanotubes Applications for Tissue Engineering. *Biomaterials* **2007**, *28*, 344–353.
6. Singh, M. K.; Shokuhfar, T.; de Almeida Gracio, J. J.; Mendes de Sousa, A. C.; Da Fonte Fereira, J. M.; Garmestani, H.; Ahzi, S. Hydroxyapatite Modified with Carbon Nanotubes-Reinforced Poly(methyl methancrylate): A Novel Nanocomposite Materials for Biomedical Applications. *Adv. Funct. Mater.* **2008**, *9999*, 1–7.
7. Raph, P. C.; Singh, B. P.; Besra, L.; Bhattacharjee, S. Multiwalled Carbon Nanotubes Reinforced Hydroxyapatite–Chitosan Composite Coating on Ti Metal: Corrosion and Mechanical Properties. *J. Am. Ceram. Soc.* **2012**, *95*, 2725.
8. Niu, L.; Kua, H.; Chua, D. H. C. Bonelike Apatite Formation Utilizing Carbon Nanotubes as Template. *Langmuir* **2010**, *26*, 4069–4073.
9. Zhao, L.; Gao, L. Novel *In Situ* Synthesis of MWNTs-Hydroxyapatite Composites. *Carbon* **2002**, *42*, 38–42.
10. Kim, S.; Ku, S. H.; Lim, S. Y.; Kim, J. H.; Park, C. B. Graphene–Biomaterial Hybrid Materials. *Adv. Mater.* **2011**, *23*, 2009–2014.
11. Brown, B. W.; Brown, P. W.; Constantz, B. *Hydroxyapatite and Related Materials*; CRC Press: Boca Raton, FL, 1994.
12. Hartgerink, J. D.; Beniash, E.; Stupp, S. I. Self-Assembly and Mineralization of Peptide-Amphiphile Nanofibers. *Science* **2001**, *294*, 1684–1688.
13. Elías, A. L.; Rodríguez-Manzo, J. A.; McCartney, M. R.; Golberg, D.; Zamudio, A.; Baltazar, S. E.; López-Urías, F.; Munoz-Sandoval, E.; Gu, L.; Tang, C. C.; *et al.* Production and Characterization of Single-Crystal FeCo Nanowires Inside Carbon Nanotubes. *Nano Lett.* **2005**, *5*, 467–472.
14. Jankovič, L.; Gournis, D.; Trikalitis, P. N.; Arfaoui, L.; Cren, T.; Rudolf, P.; Sage, M.-H.; Palstra, T. M.; Kooi, B.; Hosson, J. D.; *et al.* Carbon Nanotubes Encapsulating Superconducting Single-Crystalline Tin Nanowires. *Nano Lett.* **2006**, *6*, 1131–1135.
15. Jevtić, M.; Mitrić, M.; Škapin, S.; Jančar, B.; Ignjatović, N.; Uskoković, D. Crystal Structure of Hydroxyapatite Nanorods Synthesized by Sonochemical Homogeneous Precipitation. *Cryst. Growth Des.* **2008**, *8*, 2217–2222.
16. Kouklin, N.; Tzolov, M.; Straus, D.; Yin, A.; Xu, J. M. Infrared Absorption Properties of Carbon Nanotubes Synthesized by Chemical Vapor Deposition. *Appl. Phys. Lett.* **2004**, *85*, 4463–4465.
17. Lu, H. B.; Chempbell, C. T.; Graham, D. J.; Ratner, B. D. Surface Characterization of Hydroxyapatite and Related Calcium Phosphates by XPS and TOF-SIMS. *Anal. Chem.* **2000**, *72*, 2886–2894.
18. Hinshelwood, C. N.; Topley, B. The Unimolecular Decomposition of Phosphine. *J. Chem. Soc. Trans.* **1924**, *125*, 393–406.
19. Zhang, Y.; Tham, F. S.; Nixon, J. F.; Taylor, C.; Green, J. C.; Reed, C. A. The Low Basicity of Phosphabenzenes: First Examples of Protonation, Alkylation, and Silylation Reactions. *Angew. Chem., Int. Ed.* **2008**, *47*, 3801–3804.
20. Barbucci, R. *Integrated Biomaterials Science*; Kluwer Academic/Plenum Publishers: New York, 2002.
21. Michail, N. N.; Faris, F. S.; Hassan, M. W. A.; Kerlous, R. G. Improvement of Leguminous Vegetables Production in Calcareous Soil by Addition of Some Acidifying Materials. *Fert. Res.* **1996**, *43*, 87–91.
22. Kessler, R. J.; Vaughn, D. A. Divalent Metal Is Required for Both Phosphate Transport and Phosphate Binding to Phosphorin, a Proteolipid Isolated from Brush-Border Membrane Vesicles. *J. Biol. Chem.* **1984**, *259*, 9059–9063.

23. Nelson, B. N.; Exarhos, G. J. Infrared Studies of Glass Films Exposed to NH_3, PH_3, and H_2S. *J. Phys. Chem.* **1980**, *84*, 2867–2871.
24. Dijk, S.; Dean, D. D.; Liu, Y.; Zhao, Y.; Chirgwin, J. M.; Schwartz, Z.; Boyan, B. D. Purification, Amino Acid Sequence, and cDNA Sequence of a Novel Calcium-Precipitating Proteolipid Involved in Calcification of *Corynebacterium matruchotii*. *Calcif. Tissue Int.* **1998**, *62*, 350–358.
25. Anderson, Ö. H.; Kangasniemi, I. Calcium Phosphate Formation at the Surface of Bioactive Glass *in Vitro*. *J. Biomed. Mater. Res.* **1991**, *25*, 1019–1030.
26. Xu, T. T.; Zheng, J.-G.; Nicholls, A. W.; Stankovich, S.; Piner, R. D.; Ruoff, R. D. Single-Crystal Calcium Hexaboride Nanowires: Synthesis and Characterization. *Nano Lett.* **2004**, *4*, 2051–2055.
27. Tang, R.; Darragh, M.; Orime, C. A.; Guan, X.; Hoyer, J. R.; Nancollas, G. H. Control of Biomineralization Dynamics by Interfacial Energies. *Angew. Chem.* **2005**, *117*, 3764–3768.
28. Yang, Y.; Cui, Q.; Sahai, N. How Does Bone Sialoprotein Promote the Nucleation of Hydroxyapatite? A Molecular Dynamics Study Using Model Peptides of Different Comformations. *Langmuir* **2010**, *26*, 9848–9859.
29. Tao, J.; Pan, H.; Zeng, Y.; Xu, X.; Tang, R. Role of Amorphous Calcium Phosphate and Biological Additives in the Assembly of Hydroxyapatite Nanoparticles. *J. Phys. Chem. B* **2007**, *111*, 13410–13418.
30. Koutsopoulos, S.; Dala, E. Hydroxyapatite Crystallization in the Presence of Amino Acids with Uncharged Polar Side Groups: Glycine, Cysteine, Cystine, and Glutamine. *Langmuir* **2001**, *17*, 1074–1079.
31. Reppe, W.; Kutepow, N.; Magin, A. Cyclization of Acetylenic Compounds. *Angew. Chem., Int. Ed. Engl.* **1969**, *8*, 727–733.
32. Setlur, A. A.; Dai, J. Y.; Lauerhaas, J. M.; Chang, R. P. H. Formation of Filled Carbon Nanotubes and Nanoparticles Using Polycyclic Aromatic Hydrocarbon Molecules. *Carbon* **1998**, *36*, 721–723.
33. Watson, M. D.; Fechtenkötter, A.; Müllen, K. Big Is Beautiful—"Aromaticity" Revisited from the Viewpoint of Macromolecular and Supermolecular Benzene Chemistry. *Chem. Rev.* **2001**, *101*, 1267–1300.
34. Rümmeli, M. H.; Kramberger, C.; Grüneis, A.; Ayala, P.; Gemming, T.; Büchner, B.; Pichler, T. On the Graphitization Nature of Oxides for the Formation of Carbon Nanostructures. *Chem. Mater.* **2007**, *19*, 4105–4107.
35. Magrez, A.; Seo, J. W.; Kuznetsov, V. L.; Forró, L. Evidence of an Equimolar C_2H_2-CO_2 Reaction in the Synthesis of Carbon Nanotubes. *Angew. Chem., Int. Ed.* **2007**, *46*, 441–444.
36. Henning, P. A.; Landa-Cánovas, A. R.; Larsson, A.; Lidin, S. Elucidation of the Crystal Structure of Oxyapatite by High-Resolution Electron Microscopy. *Acta Crystallogr., Sect. B* **1999**, *55*, 170–176.
37. Okpalugo, T. I. T.; McKenna, E.; Magee, A. C.; McLaughlin, J.; Brown, N. M. D. The MTT Assays of Bovine Retinal Pericytes and Human Microvascular Endothelial Cells on DLC and Si-DLC-Coated TCPS. *J. Biomed. Mater. Res.* **2004**, *71A*, 201–208.
38. Michiardi, A.; Aparico, C.; Ratner, B. D.; Planell, J. A.; Gil, J. The Influence of Surface Energy on Competitive Protein Adsorption on Oxidized NiTi Surfaces. *Biomaterials* **2007**, *28*, 586–594.
39. Kennedy, S. B.; Washburn, N. R.; Simon, C. G., Jr.; Amis, E. J. Combinatorial Screen of the Effect of Surface Energy on Fibronectin-Mediated Osteoblast Adhesion, Spreading and Proliferation. *Biomaterials* **2006**, *27*, 3817–3824.
40. Dalby, M. J.; Gadegaard, N.; Tare, R.; Andar, A.; Riehle, M. O.; Herzyk, P.; Wilkinson, C. D. W.; Oreffo, R. O. C. The Control of Human Mesenchymal Cell Differentiation Using Nanoscale Symmetry and Disorder. *Nat. Mater.* **2007**, *6*, 997–1003.
41. Oh, S.; Brammer, K. S.; Li, Y. S. J.; Teng, D.; Engler, A. J.; Chien, S.; Jin, S. Stem Cell Fate Dictated Solely by Altered Nanotube Dimension. *Proc. Natl. Acad. Sci. U.S.A.* **2009**, *106*, 2130–2135.
42. Nayak, T. R.; Anderson, H.; Makam, V. S.; Khaw, C.; Bae, S.; Xu, X.; Ee, P.-L. R.; Ahn, J.-H.; Hong, B.-H.; Pastorin, G.; *et al.* Graphene for Controller and Accelerated Osteogenic Differentiation of Human Mesenchymal Stem Cells. *ACS Nano* **2011**, *5*, 4670–4678.
43. Kagan, V. E.; Konduru, N. V.; Feng, W.; Allen, B. L.; Conroy, J.; Volkov, Y.; Vlasova, I. I.; Belikova, N. A.; Yanamala, N.; Kapralov, A.; *et al.* Carbon Nanotubes Degraded by Neutrophil Myeloperoxidase Induce Less Pulmonary Inflammation. *Nat. Nanotechnol.* **2010**, *5*, 354–359.
44. Facca, S.; Lahiri, D.; Fiorence, F.; Messadeq, N.; Mainard, D.; Benkirane-Jessel, N.; Agarwal, A. *In Vivo* Osseointegration of Nano-Designed Composite Coating on Titanium Implants. *ACS Nano* **2011**, *5*, 4790–4799.
45. Usui, Y.; Aoki, K.; Narita, N.; Murakami, N.; Nakamura, I.; Nakamura, K.; Ishigaki, N.; Yamazaki, H.; Horiuchi, H.; Kato, H.; *et al.* Carbon Nanotubes with High Bone-Tissue Compatibility and Bone-Formation Acceleration Effects. *Small* **2008**, *4*, 240–246.
46. Hahn, B.; Lee, J.; Park, D.; Choi, J.; Ryu, J.; Yoon, W.; Lee, B.; Shin, D.; Kim, H. Mechanical and *In Vitro* Biological Performances of Hydroxyapatite–Carbon Nanotube Composites Coatings Deposited on Ti by Aerosol Deposition. *Acta Biomater.* **2009**, *5*, 3205–3214.
47. Park, B.; Jung, K.; Song, W.; O, B.; Ahn, S. Bending of a Carbon Nanotube in Vacuum Using a Focused Ion Beam. *Adv. Mater.* **2006**, *18*, 95–98.
48. Kim, P.; Lber, C. M. Nanotube Nanotweezers. *Science* **1999**, *286*, 2148–2150.